Chinese Chemical Letters 37 (2026) 110829

Contents lists available at ScienceDirect

Chinese Chemical Letters

journal homepage: www.elsevier.com/locate/cclet

Construction of near-infrared active nickel(II) nanoplatform for treating wound bacterial infection

Ruijing Zhang[a,b], Yangyuting Zhou[b,c], Song Gao[a,b,d,*], Jun-Long Zhang[b,*]

[a] The Institute of Spin Science and Technology, School of Chemistry and Chemical Engineering, South China University of Technology, Guangzhou 510641, China
[b] Beijing National Laboratory for Molecular Sciences, College of Chemistry and Molecular Engineering, Peking University, Beijing 100871, China
[c] College of Chemistry and Chemical Engineering, Shantou University, Shantou 515063, China
[d] School of Chemistry, Sun Yat-Sen University, Guangzhou 510275, China

ARTICLE INFO

Article history:
Received 31 October 2024
Revised 26 December 2024
Accepted 6 January 2025
Available online 6 January 2025

Keywords:
Nickel nanoplatform
Bacterial infection
Antimicrobial phototherapy
Photothermal therapy
Photocatalysis

ABSTRACT

The rise of antibiotic-resistant bacteria and the formation of biofilms are significant challenges in surgical practice, posing a serious threat to public health due to postoperative wound infections. A promising approach to tackle this issue is the combination of photothermal therapy (PTT) and chemodynamic therapy (CDT), which has shown remarkable effectiveness in treating both cancer and wound infections. In our study, we developed an innovative artificial nanoplatform called **Ni-2**@F127 by encapsulating **Ni-2** in a biocompatible Pluronic. When exposed to 880 nm laser irradiation, **Ni-2**@F127 exhibited exceptional photothermal performance, achieving a photothermal conversion efficiency of 60.4%, along with significant photocatalytic capabilities. This platform activates a Fenton-like reaction that catalyzes hydrogen peroxide (H_2O_2), producing toxic hydroxyl radicals (·OH) effectively. The synergistic effects of hyperthermia and ·OH not only destroy tumor cells but also demonstrate powerful antimicrobial activity, significantly inhibiting the growth of *Escherichia coli* and *Staphylococcus aureus* (*S. aureus*) *in vitro* under near-infrared (NIR) irradiation. Importantly, in animal models, **Ni-2**@F127 effectively eliminates *S. aureus* from deep tissues in cases of subcutaneous abscesses and knife injuries, significantly accelerating abscess resolution and promoting wound healing. The compelling evidence suggests that Ni-based metal complexes could serve as transformative antibacterial agents in phototherapy, unlocking vast potential for their application in wound healing and the treatment of bacterial infections.

© 2026 Published by Elsevier B.V. on behalf of Chinese Chemical Society and Institute of Materia Medica, Chinese Academy of Medical Sciences.

Each year, hundreds of millions of individuals worldwide experience skin wounds, which can be either external (such as abrasions, surgical cuts, or burns) or endogenous (linked to conditions like diabetes and vascular diseases) [1–3]. These wounds present a significant challenge to public health. A particular concern in wound management is the risk of infection, often caused by the colonization of bacteria and other microorganisms at the wound site [4–6]. Although various antibiotics are routinely employed in clinical practice, their widespread use has contributed to the rise of antibiotic resistance, thereby diminishing their efficacy and exacerbating the issue of drug-resistant bacteria [7–10]. Additionally, bacteria can evade treatment and hostile conditions by forming biofilms, which serve as protective enclaves for the bacterial cells [11–13]. In light of the urgent emergence of drug-resistant bacteria and biofilm formation, there is an increasing need to develop innovative therapeutic strategies that leverage external stimuli to address these challenges effectively.

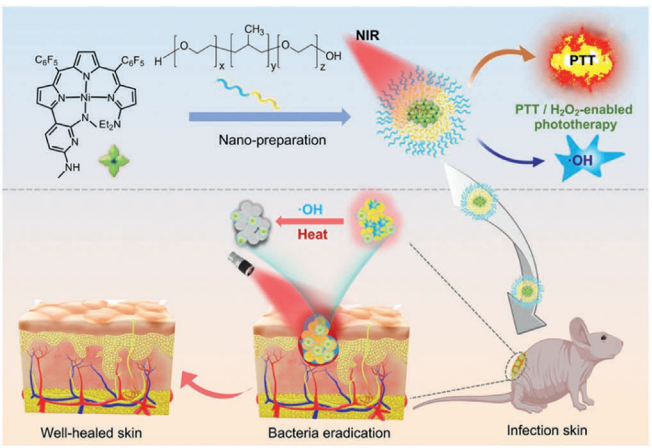
Photothermal therapy (PTT) has garnered significant attention due to its unique features, including its noninvasive nature, tissue permeability, and the ability for spatiotemporal adjustment [14–17]. PTT is widely recognized as an effective and precise strategy for local thermal sterilization, which has the advantage that the heat generated by efficient photothermal conversion disrupts bacterial structure in wound tissue, resulting in bacterial inactivation through protein denaturation and enzymatic decomposition [18–20]. However, one major drawback of PTT is that it often requires 60 °C or higher temperatures to kill bacteria effectively. Such high temperatures can cause thermal damage to surrounding tissues and may even trigger new inflammation [21]. This limitation highlights the need to develop safer and more effective phototherapy

* Corresponding authors at: Beijing National Laboratory for Molecular Sciences, College of Chemistry and Molecular Engineering, Peking University, Beijing 100871, China.
E-mail addresses: gaosong@scut.edu.cn (S. Gao), zhangjunlong@pku.edu.cn (J.-L. Zhang).

https://doi.org/10.1016/j.cclet.2025.110829
1001-8417/© 2026 Published by Elsevier B.V. on behalf of Chinese Chemical Society and Institute of Materia Medica, Chinese Academy of Medical Sciences.

strategies for rapid antimicrobial treatment. Recent studies suggest that combining PTT with other therapies could enhance antimicrobial activity through synergistic effects [22–27]. Reactive oxygen species (ROS) possess strong oxidative properties that can combat bacteria and biofilms by promoting intracellular oxidation, denaturing proteins, oxidizing lipids, and disrupting bacterial biofilm membranes and matrix structures. Highly reactive ROS are typically produced in photodynamic therapy (PDT) [28,29], sonodynamic therapy (SDT) [30], and *via* Fenton or Fenton-like reactions, such as chemodynamic therapy (CDT) and photocatalytic therapy (PCT) [31,32]. However, PDT and SDT primarily depend on the availability of endogenous oxygen, which limits their effectiveness and penetration *in vivo* [33–35]. Notably, the microenvironment of a wound infection often contains excessive hydrogen peroxide (H_2O_2), which can worsen bacterial infections and impede the healing process [36–38]. As a non-antibiotic alternative, Fenton or Fenton-like reactions utilize metal platforms with peroxidase-like activity to catalyze the production of large quantities of hydroxyl radicals (•OH) from H_2O_2. While these radicals effectively destroy bacteria, their short lifespan and limited diffusion distance can reduce their effectiveness against infections [26,39,40]. The heat generated by PTT can enhance ROS production, while the ROS generated by Fenton-like reactions can increase the permeability and thermal sensitivity of bacterial membranes, potentially improving therapeutic efficacy. Therefore, metal-based nanoplatforms capable of delivering thermal energy and ROS are promising candidates for treating bacterial infections.

Highly efficient photothermal conversion efficiency (PCE) is essential for the development of effective antibacterial therapies. Various multifunctional nanomaterials, including Fe-, Cu-, Mn-, Mo-, and Co-based photothermal nanocatalysts, have been investigated for synergistic antibacterial treatment [26,32,41–45]. However, uncertainties regarding their structures and potential side effects have hindered their practical applications. In our previous work, we designed an innovative dual-functional, oxygen-independent phototheranostic agent, nickel(II) tripyrrin (**Ni-2**), capable of NIR photoactivation, which generates thermal energy and •OH [46]. **Ni-2** operates as a multifunctional phototherapy reagent, integrating multiple therapeutic modalities into a single molecule, thus presenting a promising theragnostic platform for antimicrobial therapy. In this study, we developed NIR-active nanomaterials, **Ni-2**@F127, as a sophisticated therapeutic platform that combines PTT and photocatalysis to effectively address bacterial infections and eliminate biofilms (Scheme 1). **Ni-2**@F127 demonstrates strong NIR absorption in the near-infrared biowindow and exhibits excellent photothermal effects (PCE = 60.4 %). Additionally, it possesses unique photocatalytic properties that facilitate the conversion of hydrogen peroxide (H_2O_2) into •OH. These characteristics indicate that **Ni-2**@F127-mediated phototherapy exerts a significant antibacterial effect against *Staphylococcus aureus* (*S. aureus*) and *Escherichia coli* (*E. coli*). Animal studies further corroborated the effectiveness of **Ni-2**@F127 in treating conditions such as subcutaneous abscesses and knife wounds, underscoring its antibacterial properties. Thus, **Ni-2**@F127, combining photocatalytic capabilities with PTT under NIR irradiation, represents a promising non-antibiotic strategy for eliminating bacterial infections.



Scheme 1. Schematic illustration of the fabrication process of nickel nanoplatform **Ni-2**@F127 for photothermal therapy combined with photocatalysis to achieve antibacterial therapy and promote wound healing *in situ*.

As our continued interest in exploring the biomedical applications of 3d transition metal complexes, we investigated the nickel complex, **Ni-2**, for its potential use in treating bacterial infections in wounds. The detailed synthetic procedures for **Ni-2** had been reported in previous work [46]. **Ni-2** exhibited remarkable enhancement in non-radiative relaxation, excellent photothermal efficacy, and photocatalytic properties, to allow the catalytic conversion from H_2O_2 to •OH. In this study, we prepared the **Ni-2**@F127 nanomaterial, as illustrated in Fig. 1A, by embedding **Ni-2** into the Pluronic F-127 matrix. As shown in Fig. 1B, dynamic light scattering (DLS) measurements revealed that the average hydrodynamic size of **Ni-2**@F127 was approximately 141.4 nm, and the transmission electron microscopy (TEM) images indicated a uniform morphology. Furthermore, we measured the absorption of **2@**F127 and **Ni-2**@F127 using a UV–vis spectrophotometer. As shown in Fig. 1C, **Ni-2**@F127 exhibited strong absorption in the near-infrared (NIR) region (700–1100 nm) compared to **2**@F127 alone. The maximum absorption for **2**@F127 and **Ni-2**@F127 were determined to be 680 nm and 910 nm, respectively. This significant redshift in the low-energy absorption bands can be attributed to the enhanced π-conjugation of ligand **2** upon coordination with the nickel metal, which is beneficial for maintaining the photothermal activity of **Ni-2**@F127. To assess biosafety and compatibility, we evaluated the viability of normal embryonic fibroblast cell lines (NHT 3T3 cells) in the presence of **Ni-2**@F127 (Fig. 1D).

The peroxidase-like catalytic and photothermal properties of **Ni-2**@F127 were thoroughly investigated (Fig. 2A). We began by assessing the generation of •OH through a **Ni-2**@F127-induced Fenton-like reaction when exposed to near-infrared (NIR) laser irradiation in the presence of H_2O_2. The production of •OH was measured using a methylene blue (MB) assay, as MB can be oxidized by •OH, resulting in a reduction of maximum absorbance at 664 nm. Notably, in the presence of **Ni-2**@F127 under NIR irradiation, a significant change in MB absorbance was observed, especially in comparison to the results obtained with **2**@F127 or the laser alone (Fig. 2B). This finding indicates that **Ni-2**@F127 in its excited state is essential for •OH generation. Furthermore, considering the exceptional photophysical characteristics and the potential for photothermal conversion of **Ni-2**@F127, we evaluated its photothermal capabilities in aqueous solutions by irradiating samples at varying concentrations. When subjected to an 880 nm laser (1.0 W/cm^2), **Ni-2**@F127 demonstrated considerable temperature changes of 17.7 °C (at 100 μmol/L) and 12.2 °C (at 50 μmol/L), highlighting that temperature variations are concentration-dependent. In contrast, only minor temperature changes (<2.5 °C) were recorded for **2**@F127 and water under identical experimental conditions (Fig. 2C). The thermal imaging results (Fig. 2D) aligned well with those obtained from thermocouple measurements. These results emphasize the remarkable photothermal effect of **Ni-2**@F127, suggesting its potential as an effective agent for PTT. In comparison to **2**@F127, the enhanced photocatalytic performance and superior photothermal effect of **Ni-2**@F127 can be attributed to the successful coordination of **2** with Ni, which modifies the excited state energy level

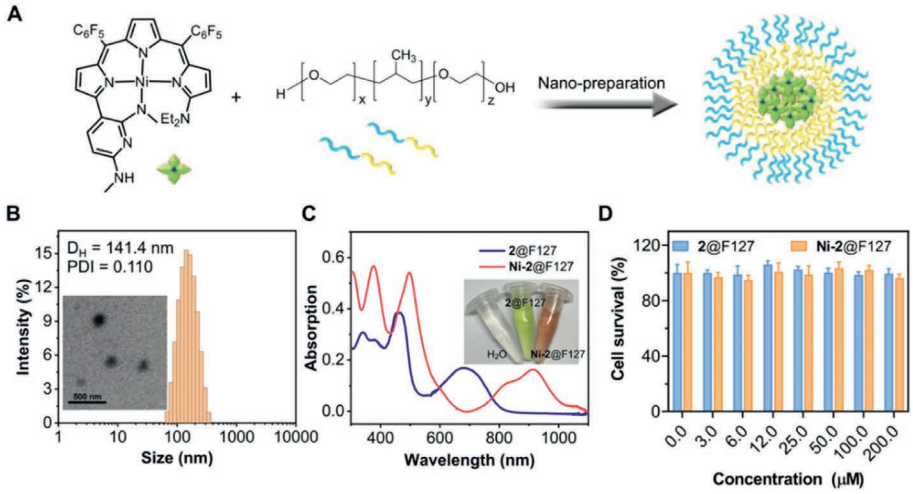


Fig. 1. Preparation and characterization of the **Ni-2**@F127. (A) Schematic diagram of the construction process for **Ni-2**@F127. (B) Hydrodynamic diameter distribution and transmission electron microscope (TEM) images (inset) obtained for **Ni-2**@F127. Scale bar: 500 nm. (C) Ultraviolet-visible spectroscopy (UV–vis) absorption spectra of **2**@F127 and **Ni-2**@F127. (Inset) The photograph of H_2O, **2**@F127 and **Ni-2**@F127 solution. (D) Viability of normal cell level (NHT 3T3 cells) incubated with **2**@F127 and **Ni-2**@F127 nanoagents in the absent of NIR laser irradiation.

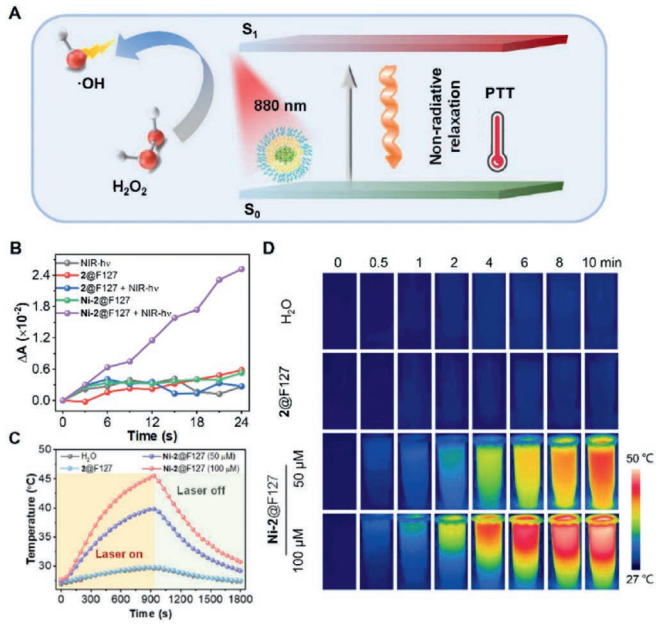


Fig. 2. Photophysical and photocatalysis studies. (A) Schematic illustration of photophysical properties and photocatalysis of **Ni-2**@F127 upon NIR photoactivation (S_0 = ground singlet state; S_1 = excited singlet state). (B) Production of ·OH as inferred from the change in MB absorbance at 664 nm under different conditions. (C) Heating curves of the H_2O, **2**@F127 (100 μmol/L), **Ni-2**@F127 (50 μmol/L), and **Ni-2**@F127 (100 μmol/L) under 880 nm laser irradiation (1.0 W/cm^2) for 15 min and then cooling to room temperature. (D) Infrared imaging of dispersions of H_2O, **2**@F127, **Ni-2**@F127.

of the **Ni-2** complex. Thus, these results indicate that **Ni-2**@F127 holds promise as a powerful antibacterial nanoagent for synergistic photocatalysis in combination with PTT.

Next, in order to better evaluate the light-controlled therapy of **Ni-2**@F127, we performed cytotoxicity experiments in HeLa cells (Fig. 3A). The Cell Counting Kit-8 (CCK-8) assay was used to evaluate the cytotoxicity of **Ni-2**@F127 against HeLa cells pre-incubated with H_2O_2. As shown in Fig. 3B, after 24 h of incubation with **2**@F127 and **Ni-2**@F127 (50 μmol/L), we observed over 85 % cell viability, indicating that the nanomaterials exhibit low cytotoxicity in the dark without NIR irradiation. However, upon exposure to light (880 nm, 1.0 W/cm^2) for 5 min, the relative viability of HeLa cells of the "**Ni-2**@F127" group decreased significantly to 16.6 %, while the **2**@F127 group still maintained high cell viability (Fig. 3C). To clearly demonstrate the therapeutic effect of **Ni-2**@F127, HeLa cells incubated with H_2O_2 were treated with various conditions and then co-stained with calcein acetoxymethyl ester (Calcein-AM) and propidium iodide (PI). Live and dead cells were stained with green and red fluorescence, respectively, and were observed using confocal laser scanning microscopy (CLSM). As shown in Fig. 3D, the cells in the "Control (PBS), PBS + Laser, **2**@F127, **2**@F127 + Laser, and **Ni-2**@F127" groups displayed abundant green fluorescence, indicating that laser exposure alone or the presence of **Ni-2**@F127 alone did not induce cell death. However, almost all cells exhibited red fluorescence after treatment with **Ni-2**@F127 under 880 nm laser irradiation, indicating significant cell death. Notably, strong green fluorescence was observed in the area without laser irradiation in the "**Ni-2**@F127 + Laser" group. These results suggest that controlled laser irradiation of **Ni-2**@F127 is effective in inducing cancer cell death. Furthermore, we assessed the impact of **Ni-2**@F127 on clone formation (Fig. 3E). A significantly reduced number of colonies was found in the "**Ni-2**@F127 + Laser" group compared to the control groups, which aligns with the previous findings. Overall, these results indicate that **Ni-2**@F127 demonstrates excellent biocompatibility and efficiently induces laser-controlled damage to cancer cells under 880 nm irradiation.

Surgical resection and phototherapy for cancer can be susceptible to bacterial infections, which are associated with various acute and chronic conditions. To prevent the development of inflammation, it is essential to implement effective antimicrobial therapy during the early stages of infection. In this study, we evaluated the antibacterial properties of **Ni-2**@F127 against antibiotic-sensitive Gram-negative *E. coli* and Gram-positive *S. aureus* (Fig. 4A). We conducted bacterial survival experiments using a PBS solution (pH 7.4) containing 100 μmol/L H_2O_2. Utilizing the standard broth microdilution method, we assessed the *in vitro* bacterial inhibition of **Ni-2**@F127. In comparison to the control group, both types of bacteria showed negligible death in the dark, regardless of the concentrations of **2**@F127 and **Ni-2**@F127 used. Additionally, laser irradiation alone did not kill the bacteria (Figs. 4B and C). However, upon exposure to 880 nm laser irradiation, the survival rates of *E. coli* and *S. aureus* decreased significantly as the concentration of **Ni-2**@F127 increased, with antibacterial rates dropping to 22.2 % and 6.41 % at a concentration of 25 μmol/L, respectively. In contrast, the concentration of **2**@F127 did not result in a significant re-

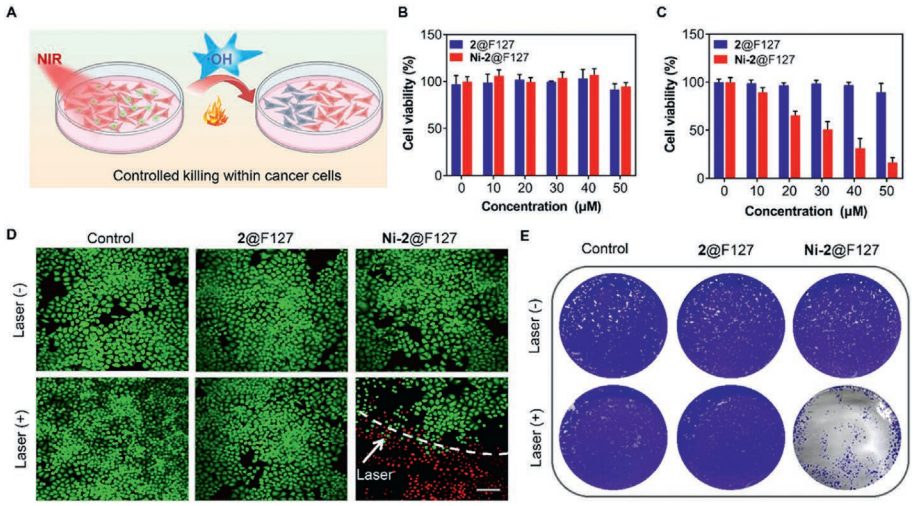


Fig. 3. *In vitro* cytotoxicity analysis of **Ni-2**@F127-mediated phototherapy in cancer cells with addition of H_2O_2 (200 μmol/L). Laser represents 880 nm laser irradiation (1.0 W/cm^2, 5 min). (A) Schematic diagram of the intracellular phototherapy including the PTT production of heat and the photocatalytic production of ·OH in cancer cells. (B) Relative cell viabilities of HeLa cells incubated with different concentration of various nanoagents under the dark or (C) in the presence of NIR laser irradiation. (D) Calcein AM (green) and propidium iodide (red) co-staining fluorescence imaging of HeLa cells after different treatments. Scale bar: 100 μm. (E) Typical photographs of colony formation of cancer cells treated with various treatments.

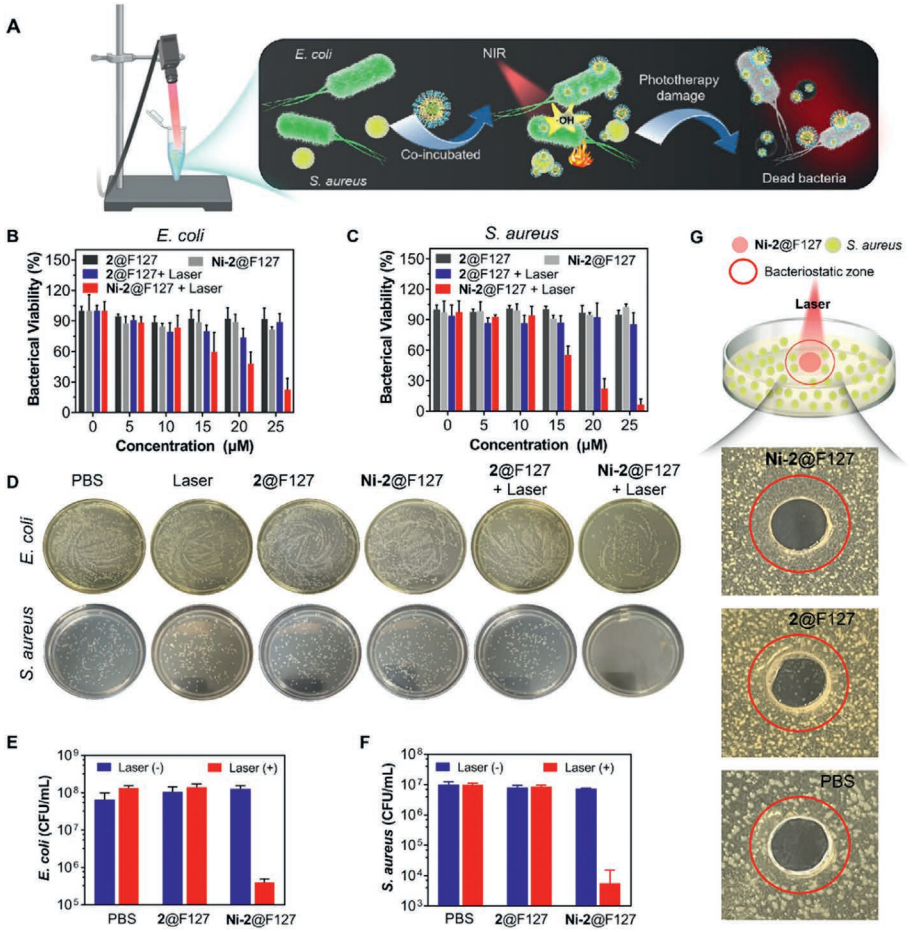


Fig. 4. *In vitro* antibacterial evaluation of **2**@F127 and **Ni-2**@F127 for phototherapy with *E. coli* and *S. aureus* treated by H_2O_2 (100 μmol/L). (A) Schematic diagram of the antibacterial therapy. Antibacterial activity of **2**@F127 and **Ni-2**@F127 toward (B) *E. coli*, and (C) *S. aureus* in the dark and under 880 nm laser irradiation (1.0 W/cm^2, 10 min). (D) Photographs of plated bacterial colonies obtained after treatment with various kinds of nanoparticles without or with laser irradiation, respectively. Antibacterial activity of (E) *E. coli* and (F) *S. aureus* after different treatments determined by the plate counting method. (G) Antibacterial zone test on agar plates against *S. aureus* recorded for **Ni-2**@F127, **2**@F127, and PBS in the presence of laser irradiation. The extent of the inhibition zone was noted in the images.

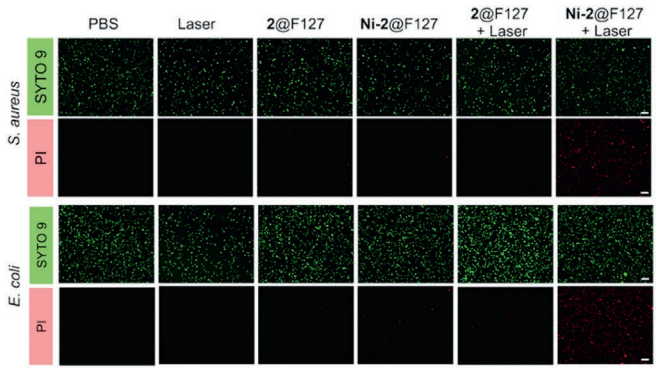


Fig. 5. CLSM images of *S. aureus* or *E. coli* stained by SYTO9 (live bacterial, green) and PI (dead bacterial, red) after different treatments. The bacterial were irradiated by an 880 nm laser light (1.0 W/cm^2, 10 min) in the presence of H_2O_2 (100 μmol/L). Scale bar: 50 μm.

duction in bacterial survival. Further evaluation of the antibacterial effect of **Ni-2**@F127 was conducted using a Luria-Bertani (LB) agar plate assay (Fig. 4D). Numerous colonies of *E. coli* and *S. aureus* survived on the LB plates in both the presence and absence of 880 nm irradiation when treated with **2**@F127. This indicated the limited bacteriostatic ability of **2**@F127. Conversely, when **Ni-2**@F127 was combined with 880 nm laser irradiation, the number of *E. coli* and *S. aureus* colonies significantly decreased and sometimes even disappeared, showing lower bacterial survival compared to the other groups (Figs. 4E and F). To further verify the antimicrobial effect of the agent, we evaluated the bacteriostatic zone. As shown in Fig. 4G, **Ni-2**@F127 created a distinct antibacterial zone, indicating its superior antimicrobial ability.

The live/dead bacterial cell viability assay was conducted to directly assess the *in vitro* antibacterial effectiveness of **Ni-2**@F127 (Fig. 5). Living and dead bacteria were stained using SYTO 9, which emits green fluorescence for living bacteria, and propidium iodide (PI), which emits red fluorescence for dead bacteria. The results showed that the bacteria in the PBS and **2**@F127 groups exhibited green fluorescence, indicating that neither laser irradiation alone nor the presence of **2**@F127 resulted in any antibacterial effect. In contrast, after treatment with **Ni-2**@F127 combined with an 880 nm laser, nearly all bacteria displayed strong red fluorescence, signifying damage to *E. coli* and *S. aureus*. These results demonstrate that **Ni-2**@F127 has excellent antibacterial properties through a combination of photothermal sterilization and catalytic production of $^{\bullet}$OH.

To investigate the phototherapy capabilities of **Ni-2**@F127 at physiological levels and to evaluate its antibacterial effects on wound healing, we established a skin abscess model on the backs of nude mice infected with *S. aureus*. All animal procedures were approved by the Institutional Animal Care and Use Committee of Sinoresearch (Beijing) Biotechnology Co., Ltd. and carried out in accordance with the requirements of the National Act on the Use of Experimental Animals (People's Republic of China). We monitored the healing progress under various conditions over a span of 10 days post-treatment (Fig. 6A). The mice were randomly divided into six groups: (1) Control; (2) Laser; (3) **2**@F127; (4) **2**@F127 + Laser; (5) **Ni-2**@F127; and (6) **Ni-2**@F127 + Laser. One day after infection, we treated the infected mice using different methods. The NIR irradiation process was recorded with a thermal imaging camera to confirm the photothermal effect of **Ni-2**@F127 *in vivo* (Fig. 6B). Under 880 nm irradiation, the wound temperature of the **Ni-2**@F127 group rapidly increased to 52 °C within 10 min. In contrast, there was no significant temperature change in the PBS group (36.9 °C) or the **2**@F127 group (39.3 °C), demonstrating the good photothermal properties of **Ni-2**@F127 (Fig. 6C).

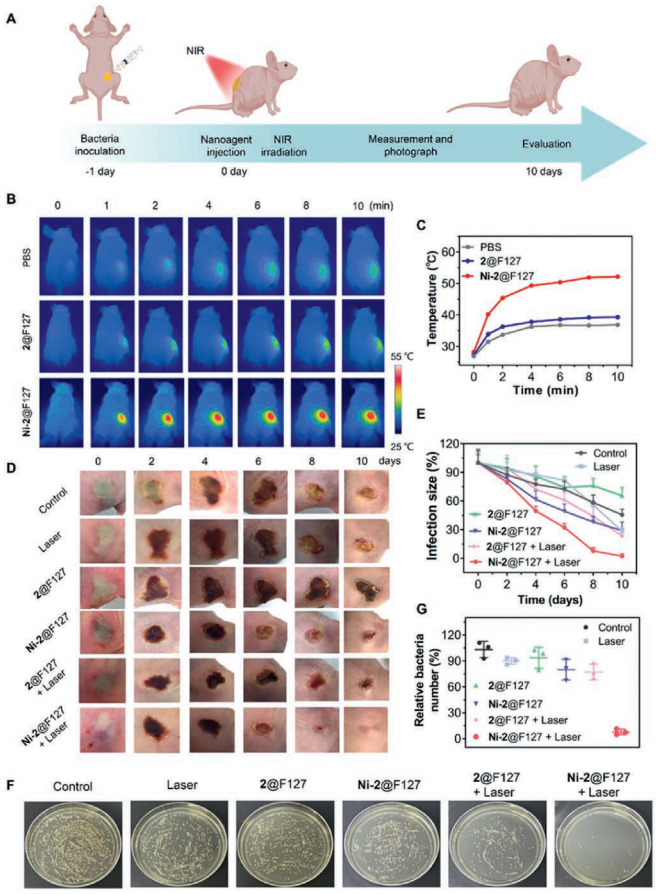


Fig. 6. NIR light-mediated antibacterial nanoplatform in abscess infection model of mice. (A) Illustrative scheme of the treatment process of the *S. aureus*-infected subcutaneous abscess. (B) Infrared thermal images and (C) temperature changes of *S. aureus*-infected mice after treatment of **2**@F127 and **Ni-2**@F127 under light irradiation (880 nm, 1.0 W/cm^2). (D) Representative photographs of *S. aureus*-infected mice after different treatments for 10 days: Control, Laser, **2**@F127, **Ni-2**@F127, **2**@F127 + Laser, and **Ni-2**@F127 + Laser. (E) Quantification of the infected area. (F) Photographs of plated bacterial colonies obtained from infected skin tissues of mice in the six treatment groups on day 10. (G) Relative bacteria number of the subcutaneous abscess on day 10.

Photographs of the wounds taken on days 0, 2, 4, 6, 8, and 10 indicated that the **Ni-2**@F127 + Laser group exhibited significant improvement in wound healing, achieving the fastest healing rate with the least edema (Fig. 6D). By day 10, compared to the Control, Laser, **2**@F127, **2**@F127 + Laser, and **Ni-2**@F127 groups, which displayed severely damaged wounds, the wound healing in the **Ni-2**@F127 + Laser group was significantly accelerated (Fig. 6E). The relative wound size in the **Ni-2**@F127 + Laser group was substantially smaller than in the PBS group, suggesting that **Ni-2**@F127-based phototherapy enhances abscess wound healing. On the 10th day of infection, we evaluated the antimicrobial efficiency of **Ni-2**@F127 by collecting bacteria from the wound sites. As shown in Fig. 6F, the colony formation and quantitative analysis indicated that the **Ni-2**@F127 + Laser group had the lowest bacterial count compared to the other groups, confirming that this group experienced accelerated wound healing through effective antibacterial activity (Fig. 6G). Additionally, there was negligible weight change observed in the mice across all groups throughout the treatment process (Fig. S1 in Supporting information), indicating the *in vivo* safety of the nanomaterials for treating drug-resistant bacteria-infected wounds.

The primary challenge during the postoperative healing process was managing bacterial infection at the wound site [47]. Fig. 7

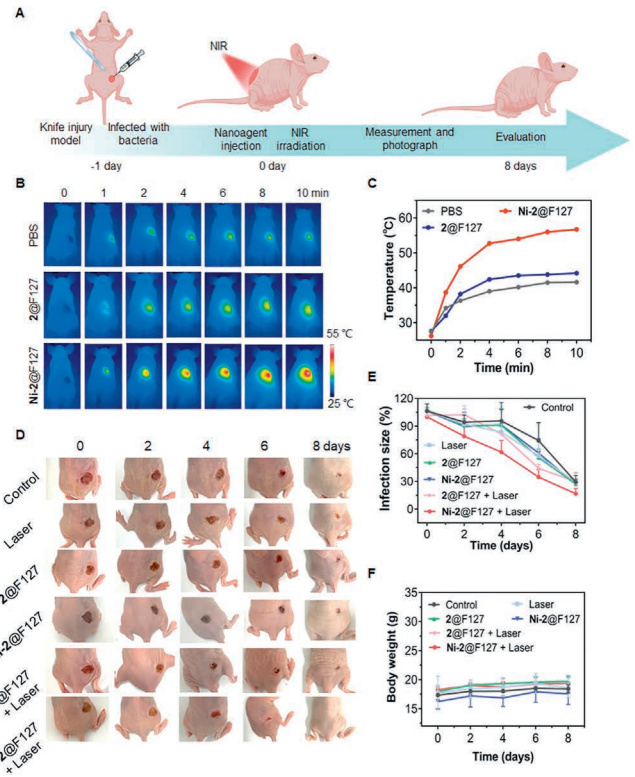


Fig. 7. Effect of the **Ni-2**@F127-mediad phototherapy in promoting skin knife wound healing *in vivo*. (A) Schematic of the *S. aureus*-infected knife wound and the timeline of animal experiments used to test the therapeutic effects of photoagents. (B) Infrared thermal images of samples under NIR irradiation *in vivo*. (C) Heating curves of samples *in vivo*. (D) Representative photographs of *S. aureus*-infected knife mice of Control, Laser, **2**@F127, **Ni-2**@F127, **2**@F127 + Laser, and **Ni-2**@F127 + Laser groups. (E) Quantification of the wound infected size and (F) animal body weight.

demonstrates the use of a **Ni-2**@F127-based therapeutic platform for healing knife injuries. As shown in Fig. 7A, initially, a round wound approximately 7 mm in diameter was created by making nicks on the backs of female BALB/c nude mice. Subsequently, an infected wound model was established by applying 20 μL of *S. aureus* suspensions with a cell density of 5.0×10^7 CFU/mL. After allowing the bacterial infection to persist for 24 h, the mice were randomly divided into six treatment groups: (1) Control; (2) Laser; (3) **2**@F127; (4) **2**@F127 + Laser; (5) **Ni-2**@F127; and (6) **Ni-2**@F127 + Laser. Upon irradiation with an 880 nm laser, the temperature at the knife injury wound treated with **Ni-2**@F127 significantly increased, reaching 55 °C, compared to the PBS and **2**@F127 groups (Figs. 7B and C). During the treatment, the trauma area was photographed and measured (Fig. 7D). Fig. 7E presents the trends in the closure of *S. aureus*-infected wounds and changes in escharosis across the different groups. In the Control, Laser, and **2**@F127 groups, clear bacterial deposits and signs of suppuration were observed throughout the treatment period, indicating prolonged bacterial presence which hindered wound closure. Notably, the wounds in the **Ni-2**@F127 + Laser group completely healed within 8 days. In contrast, the other groups, including **Ni-2**@F127 and **2**@F127 + Laser, exhibited unhealed wounds. This was attributed to the synergistic effects of reactive oxygen species (ROS) along with local mild heat. The body weight of each mouse was recorded, showing no statistically significant differences among the six groups (Fig. 7F).

On day 8, we collected and pathologically analyzed the dermal tissues around the original bacterial-infected wounds from the different groups to investigate the microscopic changes in the wound healing process (Fig. 8A). In the Control (PBS), Laser, **2**@F127,

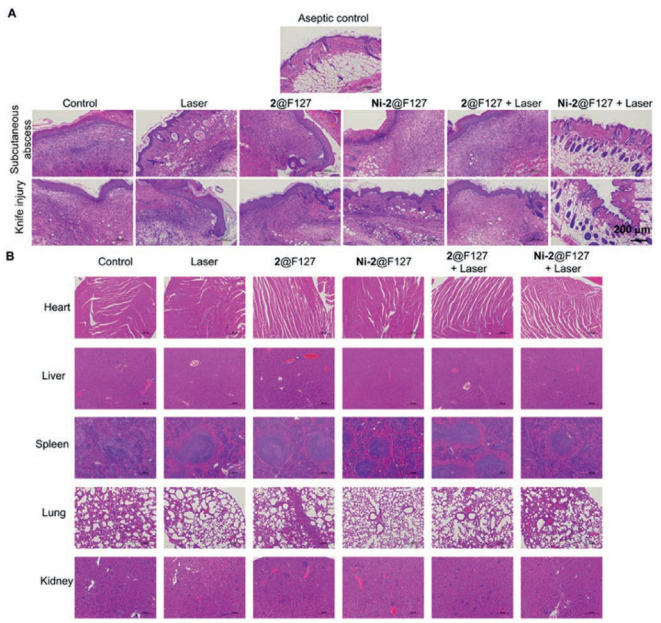


Fig. 8. Representative images of hematoxylin and eosin (H&E). (A) Histological analysis of skin tissue sections of infected mice after completion of the *in vivo* antibacterial activity experiment by H&E staining. Skin tissue from uninfected mice served as a healthy control. (B) H&E stained images of major organs of treated mice. Scale bar: 200 μm.

Ni-2@F127, and **2**@F127 + Laser groups, we observed a significant presence of inflammatory cells, the absence of intact hair follicles, neutrophil accumulation, and thickened epidermis. In contrast, the **Ni-2**@F127 + Laser group showed less severe inflammation, along with more new capillaries and hair follicles in the healed epithelial tissue compared to the other groups, resembling the healthy control group. These results suggest that **Ni-2**@F127 with laser irradiation possesses effective antibacterial properties against bacterial infections and accelerates wound healing. Additionally, we examined major organs, including the heart, liver, spleen, lungs, and kidneys, from the treated mice through H&E staining, and found no significant inflammatory or pathological damage (Fig. 8B). Overall, these results highlight the remarkable postoperative wound healing effects of the **Ni-2**@F127-based therapeutic platform.

In summary, we developed a simple yet multifunctional photocontrolled nanoplatform, **Ni-2**@F127, which exhibits strong absorption in the NIR window and possesses versatile properties. It demonstrates an excellent photothermal effect and photocatalytic properties, enabling efficient acceleration of wound healing in cases of bacterial infections. Both *in vitro* and *in vivo* studies confirm the excellent biocompatibility of **Ni-2**@F127, along with its remarkable phototherapeutic capabilities, including both photocatalytic and photothermal effects. Results from cancer cell treatments using **Ni-2**@F127 phototherapy indicate that this nanoplatform, which offers improved photocontrol, has a strong antiproliferative effect on tumor cells. Notably, experiments involving subcutaneous abscesses and knife injuries infected with bacteria further illustrate the outstanding therapeutic potential of **Ni-2**@F127. These results suggest a promising clinical application for this combined phototherapy strategy based on a nickel-based nanoplatform in treating bacterial infections, while also expanding the biological applications of chemical catalysis and photothermal effects.

Declaration of competing interest

The authors declare that they have no known competing financial interests or personal relationships that could have appeared to influence the work reported in this paper.

CRediT authorship contribution statement

Ruijing Zhang: Writing – original draft, Visualization, Validation, Software, Project administration, Methodology, Formal analysis, Data curation, Conceptualization. **Yangyuting Zhou:** Validation, Investigation, Data curation. **Song Gao:** Writing – review & editing, Supervision, Conceptualization. **Jun-Long Zhang:** Writing – review & editing, Supervision, Resources, Project administration, Funding acquisition, Conceptualization.

Acknowledgments

We acknowledge financial support from the National Scientific Foundation of China (NSFC, Nos. 21571007, 21621061, 21778002 and 21861162008). This work was supported by the High-performance Computing Platform of Peking University. This work was also supported by the Analytical Instrumentation Center of Peking University/the Center for Physicochemical Analysis and Measurements in ICCAS.

Supplementary materials

Supplementary material associated with this article can be found, in the online version, at doi:10.1016/j.cclet.2025.110829.

References

[1] C.K. Sen, G.M. Gordillo, S. Roy, et al., Wound Repair Regen. 17 (2009) 763–771.
[2] Y.P. Liang, J.H. He, B.L. Guo, ACS Nano 15 (2021) 12687–12722.
[3] I. Negut, V. Grumezescu, A.M. Grumezescu, Molecules 23 (2018) 2392.
[4] S.G. Deeks, J. Overbaugh, A. Phillips, S. Buchbinder, Nat. Rev. Dis. Primers 1 (2015) 15035.
[5] K.E. Jones, N.G. Patel, M.A. Levy, et al., Nature 451 (2008) 990–993.
[6] J.E. Cefalu, K.M. Barrier, A.H. Davis, Crit. Care Nurs. Clin. N. Am. 29 (2017) 81–96.
[7] R.L. Rosa, H.K. Johansen, S. Molin, Antibiotics 11 (2022) 419.
[8] C. Willyard, Nature 543 (2017) 15.
[9] Q. Pang, Z. Jiang, K. Wu, R. Hou, Y. Zhu, Antibiotics 12 (2023) 351.
[10] D.I. Andersson, D. Hughes, Nat. Rev. Microbiol. 8 (2010) 260–271.
[11] Y. Song, Q. Sun, J. Luo, et al., Nano-Micro Lett. 14 (2022) 83.
[12] S. Hao, H. Han, Z. Yang, et al., Nano-Micro Lett. 14 (2022) 178.
[13] C.J. Murray, K.S. Ikuta, F. Sharara, et al., Lancet 399 (2022) 629–655.
[14] X. Li, J.F. Lovell, J. Yoon, X. Chen, Nat. Rev. Clin. Oncol. 17 (2020) 657–674.
[15] L. Gai, R. Zhang, X. Shi, et al., Chem. Sci. 14 (2023) 1434–1442.
[16] Y. Yao, G. Ran, C.L. Hou, et al., J. Am. Chem. Soc. 144 (2022) 7346–7356.
[17] Y. Xiong, Y. Rao, J. Hu, Z. Luo, C. Chen, Adv. Mater. (2023) 2305140.
[18] Y. Chen, Y. Gao, Y. Chen, et al., J. Control. Release 10 (328) (2020) 251–262.
[19] V.N. Nguyen, Z. Zhao, B.Z. Tang, Chem. Soc. Rev. 51 (2022) 3324–3340.
[20] X. Li, J.F. Lovell, J. Yoon, X. Chen, Nat. Rev. Clin. Oncol. 17 (2020) 657–674.
[21] K. Yang, S. Zhao, B. Li, et al., Coord. Chem. Rev. 454 (2022) 214330.
[22] P. Manivasagan, J. Kim, E.S. Jang, Coord. Chem. Rev. 470 (2022) 214701.
[23] M. Liu, D. He, T. Yang, et al., J. Nanobiotechnol. 16 (2018) 23.
[24] S. Yougbaré, C. Mutalik, G. Okoro, et al., Int. J. Nanomed. 16 (2021) 5831–5867.
[25] S. Cai, Y. Hao, X. Wang, et al., Adv. Funct. Mater. (2024) 2413036.
[26] P. Manivasagan, T. Thambi, A. Joe, et al., Prog. Mater. Sci. 144 (2024) 101292.
[27] N. Guo, Y. Xia, Y. Duan, et al., Chin. Chem. Lett. 34 (2023) 107542.
[28] K. Cheng, H. Wang, S. Sun, et al., Small 19 (2023) e2207868.
[29] W. Sun, X. Luo, P. Li, et al., Chin. Chem. Lett. 35 (2024) 109522.
[30] X. Lin, J. Song, X. Chen, H. Yang, Angew. Chem. Int. Ed. 59 (2020) 14212–14233.
[31] B. Ran, L. Ran, Z. Wang, et al., Chem. Rev. 123 (2023) 12371–12430.
[32] N. Yang, C. Cao, X. Lv, et al., BMEMat 1 (2023) e12005.
[33] M. Kolarikova, B. Hosikova, H. Dilenko, et al., Med. Res. Rev. 43 (2023) 717–774.
[34] Z. Gong, Z. Dai, Adv. Sci. 8 (2021) 2002178 (Weinh).
[35] R. Zhang, Q. Zeng, X. Li, D. Xing, T. Zhang, Biomaterials 275 (2021) 120993.
[36] G. Zhu, Q. Wang, S. Lu, Y. Niu, Med. Princ. Pract. 26 (2017) 301–308.
[37] J. Huang, Y. Zheng, H. Niu, et al., Adv. Healthc. Mater. 13 (2024) e2302328.
[38] D. Xian, J. Song, L. Yang, et al., Oxid. Med. Cell. Longev. 2019 (2019) 2304018.
[39] P. Zhao, H. Li, W. Bu, Angew. Chem. Int. Ed. 62 (2023) e202210415.
[40] Z. Tang, Y. Liu, M. He, W. Bu, Angew. Chem. Int. Ed. 58 (2019) 946–956.
[41] Y. Fan, S. Liu, Y. Yi, H. Rong, J. Zhang, ACS Nano 15 (2021) 2005–2037.
[42] X. Wang, C. Zhang, L. He, et al., J. Nanobiotechnol. 21 (2023) 446.
[43] L. Song, K. Luo, C. Liu, et al., J. Mater. Chem. B 12 (2024) 4975–4987.
[44] P. Hu, Z. Jia, S. Zhao, et al., Adv. Healthc. Mater. 13 (2024) e2401551.
[45] X. He, Y. Lv, Y. Lin, et al., Adv. Mater. 36 (2024) e2400366.
[46] R. Zhang, H. Xu, Y. Yao, et al., J. Am. Chem. Soc. 145 (2023) 23257–23274.
[47] A. Uberoi, A.M. Vangi, E.A. Grice, Nat. Rev. Microbiol. 22 (2024) 507–521.